High-Resolution Luminescence and Absorption Spectroscopy of Cs_2GeF_6:Os^{4+}

Markus Wermuth,[†] Christian Reber,[‡] and Hans U. Güdel*,[†]

Departement für Chemie und Biochemie, Universität Bern, Freiestrasse 3, 3000 Bern 9, Switzerland, and Département de chimie, Université de Montréal, Montréal QC H3C 3J7, Canada

Received December 6, 2000

The luminescence spectrum of the Os^{4+} dopant ion occupying O_h sites of the Cs_2GeF_6 host shows three sets of resolved transitions in the near-infrared at approximately 12000, 9000, and 6700 cm^{-1}, corresponding to intraconfigurational transitions between the $^1T_{2g}$ lowest excited electronic state and the Γ_1, Γ_4, and Γ_5/Γ_3 spinor levels of the $^3T_{1g}$ ground state, respectively. The octahedral $OsF_6{}^{2-}$ chromophore does not emit from higher excited states, in contrast to related chloride and bromide host lattices, where several excited states show luminescence. The highly resolved single-crystal luminescence and absorption spectra are rationalized with ligand field parameters $10\ Dq = 24570\ cm^{-1}$, $B = 500\ cm^{-1}$, $C = 2380\ cm^{-1}$, $\zeta = 3000\ cm^{-1}$. Transition intensities reveal an intermediate coupling situation for $OsF_6{}^{2-}$: Whereas they generally follow the selection rules derived in the L−S coupling scheme, additional information can be gained from the j−j coupling limit. The resolved vibronic structure allows the identification of the most efficient ungerade parity enabling modes (vibronic origins) and shows that progressions along the a_{1g}, e_g, and t_{2g} modes occur for some transitions.

1. Introduction

Second- and third-row transition-metal ions and their complexes have very different chemical and physical properties from first-row transition-metal ions, but they have not been as extensively investigated by optical spectroscopic techniques.[1,2] A number of publications describe the optical spectroscopy of second- and third-row ions doped into halide lattices,[1] but even some of the most fundamental chromophores, such as the exactly octahedral $OsF_6{}^{2-}$ unit investigated here, have not been examined in detail.

Complexes of second- and third-row transition-metal ions have strong ligand fields, a consequence of the significant overlap of their large 4d and 5d orbitals with the adjacent ligand orbitals. In addition, spin−orbit coupling is a very important effect in the heavier transition-metal ions, larger by at least 1 order of magnitude than for corresponding 3d ions.[3] This leads to distinct differences in the electronic structure of 4d and 5d transition-metal ions, and concepts commonly used for 3d ions are no longer adequate. As an example, spin−orbit coupling can no longer be treated with a low-order perturbation approach in 5d ions, as it becomes comparable in importance to the effects of the ligand field. Spin and orbitally degenerate electronic states are consequently split by several thousand wavenumbers, energy differences comparable to the separation of electronic ground and excited states in first-row compounds.[4−6]

The strong ligand field experienced by the tetravalent 5d ions leads to $t_{2g} \leftrightarrow e_g$ transitions beyond the visible spectral range into regions where they are often masked by the onset of intense charge-transfer (CT) bands. Intraconfigurational transitions, on the other hand, are observed in the visible (VIS) and near-infrared (NIR) range as very sharp bands with well-resolved vibronic structure. Luminescence can be observed from these excited states to several ground-state levels. The intraconfigurationally excited states are only weakly coupled to the lattice, leading to inefficient nonradiative relaxation processes, and to luminescence not only from the lowest excited state but also from higher excited states.[7−9]

Os^{4+} has the [Xe] $5d^4$ electron configuration, which gives rise to a spin and orbitally degenerate $^3T_{1g}$ ground state in O_h symmetry. Several excited states arise from the same electron configuration. It is thus an excellent model system to study the effects of spin−orbit coupling and the strong ligand field. Absorption, MCD, luminescence, and upconversion luminescence of Os^{4+} doped into Cs_2ZrCl_6, Cs_2ZrBr_6, and other chloride and bromide hosts have been reported.[7,8,10−18] In contrast, the spectroscopy of the fluoride analogue is much less well described in the literature. Diffuse reflectance spectra of K_2OsF_6 have been reported,[19] as well as electronic and vibrational spectra on powders of mixed fluoro−chloro $OsF_nCl_{6-n}{}^{2-}$ ($n =$

[†] Universität Bern.

[‡] Université de Montréal.

(1) Lever, A. B. P. *Inorganic Electronic Spectroscopy*, 2nd ed.; Elsevier Science Publishers: Amsterdam, 1984.

(2) Ferguson, J. In *Progress in Inorganic Chemistry*; Lippard, S. J., Ed.; Interscience: New York, 1970; Vol. 12, p 160.

(3) Lever, A. B. P.; Solomon, E. I. In *Inorganic Electronic Structure and Spectroscopy*; Lever, A. B. P., Solomon, E. I., Eds.; John Wiley & Sons: New York, 1999.

(4) Güdel, H. U.; Snellgrove, T. R. *Inorg. Chem.* **1978**, *17*, 1617.

(5) Reber, C.; Güdel, H. U.; Meyer, G.; Schleid, T.; Daul, C. A. *Inorg. Chem.* **1989**, *28*, 3249.

(6) Jacobsen, S. M.; Güdel, H. U.; Daul, C. A. *J. Am. Chem. Soc.* **1988**, *110*, 7610.

(7) Khan, S. M.; Patterson, H. H.; Engstrom, H. *Mol. Phys.* **1978**, *35*, 1623.

(8) Flint, C. D.; Paulusz, A. G. *Mol. Phys.* **1980**, *41*, 907.

(9) Flint, C. D.; Paulusz, A. G. *Mol. Phys.* **1981**, *43*, 321.

(10) Piepho, S. B.; Dickinson, J. R.; Spencer, J. A.; Schatz, P. N. *Mol. Phys.* **1972**, *24*, 609.

(11) Nims, J. L.; Patterson, H. H.; Khan, S. M.; Valencia, C. M. *Inorg. Chem.* **1973**, *12*, 1602.

(12) Inskeep, W. H.; Schwartz, R. W.; Schatz, P. N. *Mol. Phys.* **1973**, *25*, 805.

(13) Kozikowski, B. A.; Keiderling, T. A. *Mol. Phys.* **1980**, *40*, 477.

(14) Kozikowski, B. A.; Keiderling, T. A. *J. Phys. Chem.* **1983**, *87*, 4630.

(15) Schmidtke, H. H.; Lehnert, N. *Inorg. Chem.* **1998**, *37*, 6373.

(16) Wermuth, M.; Güdel, H. U. *Chem. Phys. Lett.* **1997**, *281*, 81.

(17) Wermuth, M.; Güdel, H. U. *J. Am. Chem. Soc.* **1999**, *43*, 10102.

(18) Wermuth, M.; Güdel, H. U. *J. Chem. Phys.* **2001**, *114*, 1393.

10.1021/ic001369s CCC: \$20.00

0−6) compounds.[20−22] The absorption and MCD spectra of Cs_2GeF_6:Os^{4+} are reported for energies higher than 25500 cm^{-1},[23] but it is not clear that these spectra arise from the octahedral OsF_6^{2-} chromophore. No single-crystal absorption spectra of the electronic states below 25500 cm^{-1} and no luminescence of the OsF_6^{2-} chromophore have been reported.

In the following, we report the ligand-field transitions of Cs_2GeF_6:Os^{4+} and compare them to the spectra of Os^{4+} doped into related chloride and bromide compounds. Cs_2GeF_6 crystallizes in the cubic space group *Fm*3*m* and is isostructural to Cs_2ZrCl_6 and Cs_2ZrBr_6. It offers perfectly octahedral sites for Os^{4+}. We present high-resolution single-crystal absorption, luminescence, and excitation spectra of the OsF_6^{2-} chromophore. The combination of all spectroscopic data allows us to determine the detailed ligand-field parameters necessary for the characterization of the electronic structure. We use both the L−S and the j−j coupling limits to qualitatively rationalize experimentally observed intensities of the intraconfigurational transitions. From the analysis of the well-resolved vibronic structure of these transitions we gain detailed insight on all spin−orbit components of the ground state and on the excited states arising from intraconfigurational excitations.

2. Experimental Section

2.1. Synthesis and Crystal Growth. Polypropylene and Teflon vessels were used throughout the synthesis. Cs_2GeF_6 was prepared by dissolving 1.16 g of GeO_2 (Aldrich 99.998%) in 7 mL of HF (20%, Merck pa.) with heating. A solution of 3.36 g of CsF (Heraeus 99.999%) in 5 mL of HF (20%) was added to the above solution, leading to an immediate precipitation of the product Cs_2GeF_6, which was isolated by filtration. K_2OsF_6 was kindly provided by B. Lorenzen and W. Preetz. They prepared this compound by fluorination of K_2OsCl_6 with BrF_3.[20] Crystals of Cs_2GeF_6:Os^{4+} were grown by slow evaporation at room temperature from HF (10%) solution containing the appropriate amounts of Cs_2GeF_6 and K_2OsF_6. The crystals were of good optical quality. The Os^{4+} concentration was estimated from absorption spectra assuming an identical oscillator strength of $f = 1.7 \cdot 10^{-5}$ for the 6500 cm^{-1} transition in Cs_2GeF_6:Os^{4+} and K_2OsF_6.[24] The concentration in the doped crystals was typically found to be approximately 20% of the concentration in solution. Cs_2GeF_6:(2% Os^{4+}) and Cs_2GeF_6:(0.1% Os^{4+}) crystals were investigated in the following.

2.2. Spectroscopic Measurements. Absorption spectra were recorded on a Cary 5e spectrometer (Varian) using a closed-cycle cryostat (Air Products) for cooling the sample crystal.

Luminescence spectra were obtained by using an argon-ion laser (Spectra Physics 2060-10 SA) pumped Ti:sapphire laser (Spectra Physics 3900 S) as a tunable excitation source. Wavelength control was achieved by an inchworm (Burleigh PZ 501) driven birefringent filter. The sample luminescence was dispersed by a 0.75 m monochromator (Spex 1702) and detected by a cooled photomultiplier tube (Hamamatsu 3310-01), using a photon-counting system (Stanford Research 400) or by a liquid-nitrogen-cooled germanium photodiode (ADC 403L) combined with a lock-in amplifier (Stanford Research 830). The samples were cooled in a quartz He flow tube.[25] Luminescence spectra were corrected for the sensitivity of the detection system[26] and are displayed as photon flux versus energy.

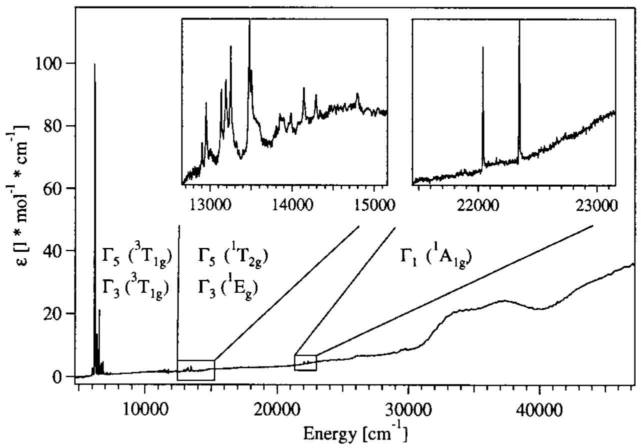

Figure 1. Absorption spectrum of Cs_2GeF_6:(2% Os^{4+}) at 15 K. The insets show an enlarged view of the energy regions of the transitions to Γ_1 ($^1A_{1g}$) and Γ_5 ($^1T_{2g}$)/Γ_3 (^1E_g), respectively.

Luminescence lifetimes were determined after pulsed excitation with the Raman shifted output (Quanta Ray RS-1, H_2 340 psi) of a dye laser (Lambda Physik FL 3002, Rhodamine 6G in methanol) pumped with the frequency doubled output of a Nd:YAG (yttrium aluminum garnet) laser (Quanta Ray DCR 3, 20 Hz). The sample luminescence was detected with the PM tube described above and recorded with a multichannel scaler (Stanford Research 430).

The data were analyzed using the Igor Pro software package (Wavemetrics).

3. Results

Figure 1 shows the 15 K absorption spectrum of Cs_2GeF_6:(2% Os^{4+}). The spectrum below 23000 cm^{-1} consists of three regions with sharp lines. Weak absorptions are observed between 23000 and 30000 cm^{-1} followed by the moderately intense absorption bands above 30000 cm^{-1}. The spectrum is dominated by the group of sharp lines around 6500 cm^{-1} assigned to the transition between the Γ_1 and Γ_5/Γ_3 ($^3T_{1g}$) ground-state spinor levels, as discussed in the following section. Two groups of weak and sharp lines observed around 13000 and 22000 cm^{-1} are assigned to Γ_5 ($^1T_{2g}$)/Γ_3 (^1E_g) and Γ_1 ($^1A_{1g}$), respectively. These multiplets are enlarged in the two insets to Figure 1. Their assignment is discussed in section 4.1, and the transition energies of the individual lines are given in Table 1. The spectrum in Figure 1 does not contain any bands with $\epsilon > 100$ $L \cdot mol^{-1} \cdot cm^{-1}$.

Figure 2 compares the 15 K absorption spectra of Cs_2ZrCl_6:(1% Os^{4+}), Cs_2ZrBr_6:(0.2% Os^{4+}), and Cs_2GeF_6:(2% Os^{4+}). Corresponding bands in the three spectra are connected with dashed lines. The very intense bands above 23000 and 17000 cm^{-1} in the chloride and bromide spectra, respectively, are assigned to charge-transfer transitions. The 22000 cm^{-1} band in the Cs_2ZrCl_6:(1% Os^{4+}) spectrum marked with an asterisk does not belong to an absorption of the octahedral $OsCl_6^{2-}$ chromophore. Its origin is unidentified.

Figure 3 shows the 15 K luminescence spectrum of Cs_2GeF_6:(0.1% Os^{4+}) excited at 13250 cm^{-1}. The three groups of lines with relative integrated photon fluxes of 0.1, 1, and 0.8 centered around 12200, 9000, and 6500 cm^{-1}, respectively, are assigned to the transitions from Γ_5 ($^1T_{2g}$) to Γ_1 ($^3T_{1g}$), Γ_4 ($^3T_{1g}$), and Γ_5/Γ_3 ($^3T_{1g}$), respectively, see the energy-level scheme in Figure 4. The total luminescence intensity of Cs_2GeF_6:(0.1% Os^{4+}) excited at 13250 cm^{-1} decreases with increasing temperature, and the intensity at 120 K is only 10% of the value observed at 15 K. The luminescence lifetime of Γ_5 ($^1T_{2g}$) strongly depends on the Os^{4+} concentration. At 15 K it decreases from 18 to 4 μs when the Os^{4+} concentration is increased from 0.1% to 2%.

---

(19) Allen, G. C.; Al-Mobarak, R.; El-Sharkawy, G. A. M.; Warren, K. D. *Inorg. Chem.* **1972**, *11*, 787.
(20) Preetz, W.; Ruf, D.; Tensfeldt, D. *Z. Naturforsch.* **1984**, *39b*, 1100.
(21) Preetz, W.; Ruf, D. *Z. Naturforsch.* **1986**, *41a*, 871.
(22) Preetz, W.; Peters, G.; Bublitz, D. *Chem. Rev.* **1996**, *96*, 977.
(23) Weiss, L. C.; McCarthy, P. J.; Jasinski, J. P.; Schatz, P. N. *Inorg. Chem.* **1978**, *17*, 2689.
(24) The K_2OsF_6 spectrum was measured on a 25 μm thick single crystal in α polarization.
(25) Krausz, E.; Tomkins, C.; Adler, H. *J. Phys. E: Sci. Instrum.* **1982**, *15*, 1167.
(26) Ejder, E. *J. Opt. Soc. Am.* **1969**, *59*, 223.

Table 1. Collection of Transition Energies Observed in the 15 K Absorption Spectrum of Cs_2GeF_6:(2% Os^{4+}) in Figure 1^a

E (cm^{-1})	Δ*E* (cm^{-1})	assignment
5956^b	0	Γ_5 ($^3T_{1g}$)
6000^b	*0*	Γ_3 ($^3T_{1g}$)
6142	186/*142*	
6156	200	v_6 (200)
6190	*190*	v_6 (200)
6205	249	v_4 (249)
6231	*231*	v_4 (241)
6373	417	$v_6 + v_5$ (217)
6410	454	$v_4 + v_5$ (205)
6427	*427*	$v_4 + v_5$ (196)
6498	542	v_3 (542)
6545	*545*	v_3 (555)
6697	741/*697*	
6735	779/*735*	
6798	842/*798*	
6831	875/*831*	
6845	889/*845*	
12693^b	0	Γ_5 ($^1T_{2g}$)
12901	208	v_6 (208)
12936^b	*0*	Γ_3 (^1E_g)
12950	257	v_4 (257)
13137	*201*	v_6 (201)
13191	*255*	v_4 (255)
13250	557	v_3 (557)
13477	*541*	v_3 (541)
13501	808/*565*	
13850	1157/*914*	
13901	1208/*965*	
13982	1289/*1046*	
14142	1449/*1206*	
14288	1595/*1352*	
14793	2100/*1857*	
21790^b	0	Γ_1 ($^1A_{1g}$)
22040	250	v_4 (250)
22345	555	v_3 (555)

^{a} The Δ*E* column contains energy differences to the electronic origins. In regions where Γ_5 and Γ_3 electronic transitions overlap, the values are given in normal and italic fonts, respectively, and both Δ*E* values are given where the assignment is not clear. The last column gives the assignments of the lines and energies (in cm^{-1}) for the vibrational modes. ^{b} Estimated values.

The individual luminescence multiplets are shown in detail in Figures 5, 6, and 7, respectively. Figure 5 shows the Γ_5 ($^1T_{2g}$) → Γ_1 ($^3T_{1g}$) luminescence multiplet excited at 13250 cm^{-1} and the excitation spectrum monitoring the Γ_5 ($^1T_{2g}$) → Γ_1 ($^3T_{1g}$) transition at 12148 cm^{-1}. The data were obtained on Cs_2GeF_6:(0.1% Os^{4+}) at 15 K. The Γ_5 ($^1T_{2g}$) and Γ_3 (^1E_g) labels indicate the positions of the two electronic origins, marked with arrows in the excitation spectrum of Figure 5. The assignment of the individual lines to the v_i ($i = 1, 2, 3, 4, 5, 6$) vibrational modes of the OsF_6^{2-} octahedron is discussed in section 4.3 and summarized in Tables 1 and 2.

Figure 6 shows an enlarged view of the 15 K Γ_5 ($^1T_{2g}$) → Γ_4 ($^3T_{1g}$) luminescence transition of Cs_2GeF_6:(0.1% Os^{4+}) excited at 13250 cm^{-1}. The assignment of the individual lines to the electronic origin, denoted as 0-0, and to the vibrational modes v_i is discussed in section 4.3 and contained in Table 2.

Figure 7 shows an enlarged view of the 15 K Γ_5 ($^1T_{2g}$) → Γ_5/Γ_3 ($^3T_{1g}$) luminescence transition of Cs_2GeF_6:(0.1% Os^{4+}) excited at 13250 cm^{-1} in comparison to the 15 K Γ_1 ($^3T_{1g}$) → Γ_5/Γ_3 ($^3T_{1g}$) absorption spectrum of Cs_2GeF_6:(2% Os^{4+}). The inverted absorption is plotted on a reversed energy axis in the bottom part of Figure 7. The displayed energy range has the same width as the luminescence spectrum shown in the top part, and the energy window is chosen in such a way that the electronic origins in absorption and luminescence occur at identical horizontal positions in the graph. The Γ_5 ($^3T_{1g}$), Γ_3 ($^3T_{1g}$) labels indicate the energetic positions of the two electronic origins, whereas the other lines are assigned to the v_i vibrational modes of the OsF_6^{2-} octahedron as discussed in section 4.3 and summarized in Tables 1 and 2.

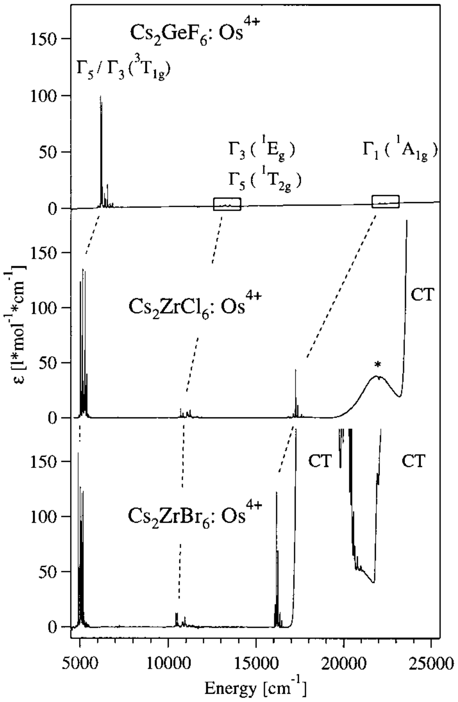

Figure 2. Absorption spectra of Cs_2GeF_6:Os^{4+}, Cs_2ZrCl_6:Os^{4+}, and Cs_2ZrBr_6:Os^{4+} at 15 K in the NIR and VIS spectral region. Corresponding bands in the three compounds are connected with dashed lines. The asterisk in the Cs_2ZrCl_6:Os^{4+} spectrum marks a band that does not belong to the octahedral $OsCl_6^{2-}$ chromophore.

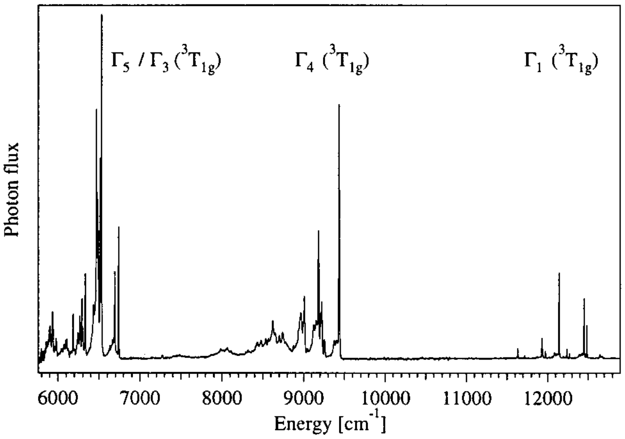

Figure 3. 15 K luminescence spectrum of Cs_2GeF_6:(0.1% Os^{4+}) excited at 13250 cm^{-1}. The assignments denote the final levels of the luminescence transitions.

4. Analysis and Discussion

4.1. Ligand-Field States of Cs_2GeF_6:Os^{4+}. The absorption, luminescence, and MCD spectra of Os^{4+} doped into chloride and bromide lattices are extensively discussed in the literature.[7,8,10−18] In contrast, the fluoride analogue has received little attention so far. The diffuse reflectance spectra of K_2OsF_6[19] and the absorption spectra on powders of mixed fluoro−chloro osmates(IV) $OsF_nCl_{6-n}^{2-}$ ($n = 0-6$) have been published.[20−22] A detailed analysis of the absorption and MCD spectroscopy

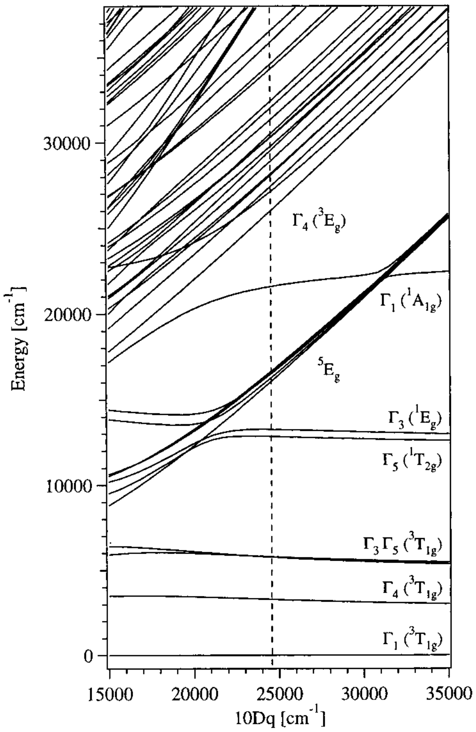

Figure 4. Part of the Tanabe–Sugano diagram for the d^4 electron configuration calculated for $B = 500$ cm^{-1}, $C = 2380$ cm^{-1}, $\zeta = 3000$ cm^{-1}. The vertical dashed line indicates the ligand-field strength deduced for Cs_2GeF_6:Os^{4+}.

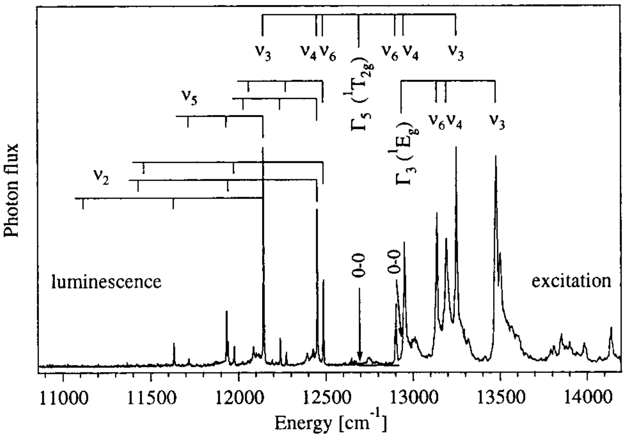

Figure 5. Enlarged view of the Γ_5 ($^1T_{2g}$) → Γ_1 ($^3T_{1g}$) luminescence transition of Cs_2GeF_6:(0.1% Os^{4+}) excited at 13250 cm^{-1} on the left-hand side compared to the excitation spectrum of the same crystal monitoring the luminescence at 12148 cm^{-1} on the right. Both spectra were measured at 15 K. The estimated positions of the electronic origins to Γ_5 ($^1T_{2g}$) and Γ_3 (^1E_g), the observed energies of the vibronic origins involving ν_6 (t_{2u}), ν_4 (t_{1u}), and ν_3 (t_{1u}) vibrations, and the progressions in the ν_5 (t_{2g}) and ν_2 (e_g) modes are indicated.

of Cs_2GeF_6:(Os^{4+}) above 25500 cm^{-1} has appeared in the literature.[23] As will be discussed below, the spectra in ref 23 do not agree with our results presented here on the same doped lattice. In contrast to the chloride and bromide analogues, no luminescence has been reported for the $OsF_6{}^{2-}$ chromophore. Os^{4+} has a $5d^4$ electron configuration and a $^3T_{1g}$ ground state in the octahedral coordination of the Ge^{4+} lattice site. The ligand-field states are given in Figure 4 for a ligand-field parameter range appropriate for the title material. The $^3T_{1g}$ electronic ground state is split by spin–orbit coupling into Γ_1, Γ_4, Γ_5, and Γ_3 with a total spread of 5000–6000 cm^{-1}.

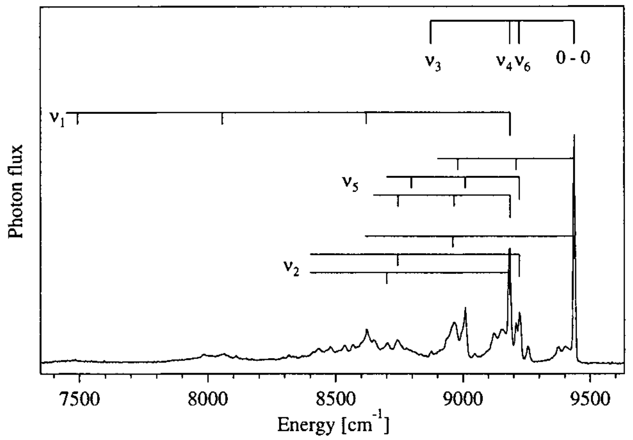

Figure 6. Enlarged view of the 15 K Γ_5 ($^1T_{2g}$) → Γ_4 ($^3T_{1g}$) luminescence transition of Cs_2GeF_6:(0.1% Os^{4+}) excited at 13250 cm^{-1}. 0-0 and ν_6 (t_{2u}), ν_4 (t_{1u}), ν_3 (t_{1u}) denote electronic and vibronic origins, respectively, and the progressions in ν_1 (a_{1g}), ν_2 (e_g), and ν_5 (t_{2g}) modes are indicated.

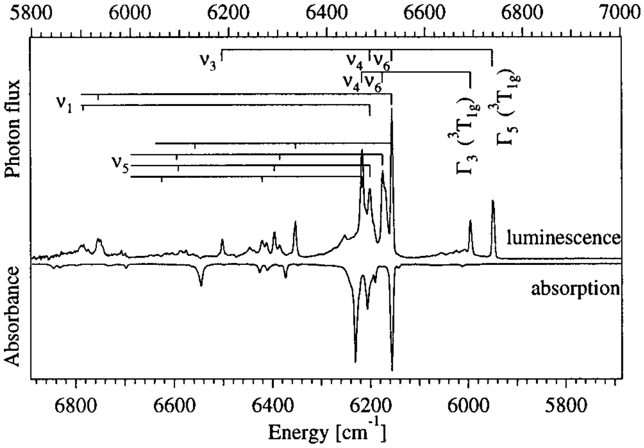

Figure 7. Enlarged view of the 15 K Γ_5 ($^1T_{2g}$) → Γ_5/Γ_3 ($^3T_{1g}$) luminescence transition of Cs_2GeF_6:(0.1% Os^{4+}) excited at 13250 cm^{-1} compared to the Γ_1 ($^3T_{1g}$) → Γ_5/Γ_3 ($^3T_{1g}$) absorption of Cs_2GeF_6:(2% Os^{4+}) at 15 K plotted on a reversed energy axis. Both the top and bottom wavenumber scales cover a range of 1200 cm^{-1}. The horizontal positions of the Γ_5/Γ_3 ($^3T_{1g}$) electronic origins are identical in the two spectra.

Figure 1 shows the 15 K overview absorption spectrum of Cs_2GeF_6:Os^{4+}. Due to the exactly octahedral coordination of Os^{4+}, all d–d electronic transitions are strictly parity-forbidden, leading to weak absorption bands dominated by vibronic origins. The absorption spectra in Figure 2 compare the fluoride, chloride, and bromide analogues of Os^{4+} doped into the isostructural hosts Cs_2GeF_6, Cs_2ZrCl_6, and Cs_2ZrBr_6, respectively. On the low-energy side all three spectra show the transitions between the lowest and highest ground-state spinor levels. Then we observe weak intraconfigurational ligand-field bands. Due to the different electronegativities of the halide ions,[27] the onsets of the charge-transfer (CT) bands vary widely. For the fluoride, they occur above 50000 cm^{-1} outside the ranges of Figures 1 and 2, and for the chloride and bromide lattices they are observed around 23000 cm^{-1} and around 17000 cm^{-1}, respectively. These charge-transfer bands are very intense and have molar absorptivities of $\epsilon \approx 6000$ L·mol^{-1}·cm^{-1}.

In this study we focus on the electronic states below 23000 cm^{-1}. This region is dominated by intraconfigurational $(t_{2g})^4$

---

(27) Jørgensen, C. K. *Orbitals in Atoms and Molecules*; Academic Press: London, 1962.

Table 2. As in Table 1 but for the Luminescence Spectrum of Cs_2GeF_6:(0.1% Os^{4+})[a]

E (cm^{-1})	ΔE (cm^{-1})	assignment
12693[b]	0	$\Gamma_5\,({}^1T_{2g}) \rightarrow \Gamma_1\,({}^3T_{1g})$
12486	207	ν_6 (207)
12451	242	ν_4 (242)
12273	420	$\nu_6 + \nu_5$ (213)
12240	453	$\nu_4 + \nu_5$ (211)
12144	549	ν_3 (549)
11974	719	$\nu_6 + \nu_2$ (512)
11941	752	$\nu_4 + \nu_2$ (510)
11933	760	$\nu_3 + \nu_5$ (211)
11717	976	$\nu_3 + 2\cdot\nu_5$ (213)
11631	1062	$\nu_3 + \nu_2$ (513)
9438[b]	0	$\Gamma_5\,({}^1T_{2g}) \rightarrow \Gamma_4\,({}^3T_{1g})$
9257	181	
9222	216	ν_6 (216)
9209	229	ν_5 (229)
9185	253	ν_4 (253)
9010	428	$\nu_6 + \nu_5$ (212)
8965	473	$\nu_4 + \nu_5$ (220)
8875	563	ν_3 (563)
8745	693	
8702	736	
8651	787	$\nu_6 + \nu_1$ (571)
8621	817	$\nu_4 + \nu_1$ (564)
8565	873	
8536	902	
8478	960	
8435	1003	
8065	1373	$\nu_4 + 2\nu_1$ (556)
6738[b]	0	$\Gamma_5\,({}^1T_{2g}) \rightarrow \Gamma_5\,({}^3T_{1g})$
6693[b]	*0*	$\Gamma_5\,({}^1T_{2g}) \rightarrow \Gamma_3\,({}^3T_{1g})$
6532	206	ν_6 (206)
6513	*180*	ν_6 (180)
6487	251	ν_4 (251)
6471	*222*	ν_4 (222)
6434	304/*259*	
6335	403	$\nu_6 + \nu_5$ (204)
6303	*390*	$\nu_6 + \nu_5$ (210)
6292	446	$\nu_4 + \nu_5$ (195)
6276	462/*417*	
6267	*426*	$\nu_4 + \nu_5$ (204)
6242	496/*451*	
6186	552	ν_3 (552)
5935	803	$\nu_6 + \nu_1$ (597)
5904	834	$\nu_4 + \nu_1$ (583)

[a] See Figure 3. [b] Estimated values.

$\rightarrow (t_{2g})^4$ transitions. The assignment of the three groups of sharp lines around 6500, 13500, and 22000 cm^{-1} to $\Gamma_5/\Gamma_3\,({}^3T_{1g})$, $\Gamma_5\,({}^1T_{2g})/\Gamma_3\,({}^1E_g)$, and $\Gamma_1\,({}^1A_{1g})$, respectively, in the fluoride absorption spectrum is straightforward from the comparison with the chloride and bromide spectra in Figure 2. The energies are in agreement with the diffuse reflectance spectra of K_2OsF_6 in ref 19, where these bands were found around 5600, 12700, and 22500 cm^{-1}, respectively. These intraconfigurationally excited states correspond to the approximately horizontal lines in the Tanabe–Sugano diagram of Figure 4, which illustrates that their energies are essentially ligand-field independent, as they arise from the same strong-field electron configuration as the ground state. The increased energies of these states compared to the chloride and bromide analogues are a consequence of the larger Racah B, C, and spin–orbit coupling ζ parameters in the fluoride. The reduction of these parameters compared to the free-ion values is qualitatively related to the covalency of the osmium(IV)–halide bonds, which is lowest in OsF_6^{2-}. The differences in the intensities of the intraconfigurational transitions are a consequence of the energetic positions of the CT states, as discussed in section 4.3.

Table 3. Comparison of Observed and Calculated Energies of the Intraconfigurational Transitions in Cs_2GeF_6:Os^{4+} [a]

	E_{obsd} (cm^{-1})	E_{calcd} (cm^{-1})	t_{2g}	e_g	contribution (%) singlet	triplet	quintet
$\Gamma_1\,({}^3T_{1g})$	0	0	3.85	0.15	6.7	85.7	7.6
$\Gamma_4\,({}^3T_{1g})$	3255	3297	3.88	0.12	0.7	91.6	7.7
$\Gamma_5\,({}^3T_{1g})$	5956	5764	3.91	0.09	14.4	82.8	2.8
$\Gamma_3\,({}^3T_{1g})$	6000	5796	3.89	0.11	9.4	84.8	5.8
$\Gamma_5\,({}^1T_{2g})$	12693	12844	3.87	0.13	81.2	14.0	4.8
$\Gamma_3\,({}^1E_g)$	12936	13258	3.86	0.14	76.3	20.7	3.0
$\Gamma_1\,({}^1A_{1g})$	21790	21593	3.68	0.32	71.0	27.8	1.2

[a] The experimental values were estimated from the observed vibronic origins, and the calculated values were obtained for $B = 500$ cm^{-1}, $C = 2380$ cm^{-1}, $\zeta = 3000$ cm^{-1} and 10 $Dq = 24570$ cm^{-1}. The t_{2g} and e_g columns give the orbital occupancies, whereas the calculated singlet, triplet, and quintet contributions to the wavefunctions are collected in the last three columns.

The formally spin-allowed transitions to the excited spinors Γ_5/Γ_3 of the ground-state ${}^3T_{1g}$ dominate the fluoride absorption spectrum. The energetic position of $\Gamma_4\,({}^3T_{1g})$ cannot be determined from the absorption spectrum but is obtained from the overview luminescence spectrum of Figure 3. The bands occurring around 12300, 9000, and 6500 cm^{-1} are assigned to $\Gamma_5\,({}^1T_{2g}) \rightarrow \Gamma_1$, Γ_4, and $\Gamma_5/\Gamma_3\,({}^3T_{1g})$, respectively. The energies of all the intraconfigurational transitions are collected in Table 3.

The determination of excited states arising from the $(t_{2g})^3\,(e_g)^1$ configuration is crucial to determine the ligand-field parameter 10 Dq. A whole series of states are expected to arise from this configuration. They are characterized by the inclined lines with a slope of 1 in Figure 4. According to Figure 4, the spin–orbit split components of ${}^5E_g$ are the lowest configurationally excited states. Transitions to these states are difficult to determine from absorption spectra as the spin- and parity-forbidden ${}^3T_{1g} \rightarrow {}^5E_g$ bands are expected to be broad and very weak. Spin-allowed transitions are expected to lie to higher energy than the ${}^3T_{1g} \rightarrow {}^5E_g$ transitions leading to broad but considerably more intense absorption bands.

Immediately above 23000 cm^{-1} weak and broad absorptions are observed in Figure 1 followed by more intense bands above 30000 cm^{-1}. We assign the weak bands to the spin-allowed interconfigurational d–d transitions of OsF_6^{2-}. The origin of the moderately intense and broad absorption bands around 35000 cm^{-1} is not completely clear. Their intensity is only partly due to the OsF_6^{2-} chromophore. A comparable absorption intensity is observed in the undoped Cs_2GeF_6 host crystal in this same spectral region. It should be noted that all the absorption bands above 23000 cm^{-1} in Figure 1 are very weak with corresponding extinction coefficients in the range of $\epsilon = 2-20$ $L\cdot mol^{-1}\cdot cm^{-1}$. This is in marked contrast to the absorption spectra published by Weiss et al. on Cs_2GeF_6:Os^{4+}.[23] They observed strong bands with $\epsilon_{max} = 1000$ $L\cdot mol^{-1}\cdot cm^{-1}$ in the range from 25000 to 33000 cm^{-1}, which they assigned to OsF_6^{2-} states originating from the $(t_{2g})^3(e_g)^1$ configuration, but were unable to detect the weaker intraconfigurational transitions below 23000 cm^{-1}. As we do not have any evidence for strong absorption bands between 25000 and 33000 cm^{-1}, but clearly observe the full set of intraconfigurational transitions expected for octahedrally coordinated Os^{4+}, we conclude that the spectra in ref 23 are dominated by a chromophore chemically different from OsF_6^{2-}. This conclusion is sustained by the experimental procedure used by Weiss et al. to obtain the Cs_2GeF_6:Os^{4+} crystals. They used H_2OsCl_6 instead of a fluoride compound as a dopant,[23] and their chromophore thus likely contains chloride.

We use the energetic positions of the intraconfigurational transitions collected in Table 3 to perform a ligand-field calculation. The energies of all intraconfigurational transitions depend only weakly on the ligand-field parameter 10 *Dq*. To determine this parameter, we use the energetic position of a state arising from a strong-field electron configuration different from the ground state. We assign the weak absorption around 26000 cm^{-1} in Figure 1 to Γ_4 (^3E_g), the lowest of a series of triplet states, see Figure 4. To perform the ligand-field calculation we used the LIGFIELD program.[28,29] We set the Racah *B* parameter to 500 cm^{-1} [19] and obtain the following parameter values optimized to reproduce the observed energies of the intraconfigurational transitions and the triplet band around 26000 cm^{-1}: $C = 2380$ cm^{-1}, $\zeta = 3000$ cm^{-1}, and 10 $Dq = 24570$ cm^{-1}.

The energies of the ligand-field states calculated with these parameters are the intersections of the solid lines with the dashed vertical line in Figure 4. The calculated energies for the intraconfigurational transitions are collected in Table 3. This parameter set places ^5E_g at around 16000 cm^{-1}, below the highest energy intraconfigurationally excited state Γ_1 ($^1A_{1g}$). In contrast to the intraconfigurationally excited states, ^5E_g is strongly coupled to the lattice and thus offers an efficient pathway for nonradiative relaxation. We believe that this is an important reason for the failure to observe Γ_1 ($^1A_{1g}$) luminescence in Cs_2GeF_6:Os^{4+}, even at temperatures as low as 15 K. This result is in contrast to the chloride and bromide analogues, where Γ_1 ($^1A_{1g}$) luminescence was observed below 150 and 100 K, respectively.[7,8,11,17,18] Due to decreased Racah parameters, ^5E_g appears to be higher in energy than Γ_1 ($^1A_{1g}$) in these latter compounds, leading to the observation of Γ_1 ($^1A_{1g}$) luminescence.

The ligand-field calculation of Allen et al.[19] based on experimental data from diffuse reflectance spectra of K_2OsF_6 was carried out with $B = 500$ cm^{-1}, $\zeta = 2900$ cm^{-1}, and 10 $Dq = 26000$ cm^{-1}. The ratio C/B was set to 4.75. This calculation shifted the position of the ^5E_g and the lowest triplet states to around 17000 and 27000 cm^{-1}, respectively, confirming the energy order established from our spectra and calculations.

Table 3 also contains characteristics of the ligand field wave functions, i.e., orbital occupancies and spin contributions. The proximity of ^5E_g and ^3E_g to $^1T_{2g}$/^1E_g and $^1A_{1g}$, respectively, leads to a considerable perturbation of the wave functions of the singlet states. Table 3 shows that the e_g occupancy of $^1T_{2g}$, ^1E_g, and $^1A_{1g}$ is between 0.1 and 0.3. Interestingly, there is e_g character also in the $^3T_{1g}$ ground state. The e_g character varies between the spinor components of $^3T_{1g}$. It is highest for Γ_1 and is smaller by almost a factor of 2 in Γ_5. This demonstrates the distinct differences between the ground-state spinor components caused by the large spin−orbit coupling parameter of 3000 cm^{-1}. Also the quintet and triplet characters in $^1T_{2g}$, ^1E_g, and $^1A_{1g}$ are astonishingly high, which is another consequence of the large spin−orbit coupling parameter.

4.2. Intensity of Luminescence Transitions to the Ground-State Spinor Levels. The luminescence spectrum in Figure 3 shows the transitions from Γ_5 ($^1T_{2g}$) to the spinor levels Γ_1, Γ_4, and Γ_5/Γ_3 of the ground state $^3T_{1g}$. In this section we focus on the relative luminescence photon fluxes of these three groups of luminescence transitions before discussing them individually in section 4.3. As the luminescence bands of Γ_5 and Γ_3 strongly overlap, we do not try to separate the two transitions and treat them as one band in the following. Integration of the luminescence bands in Figure 3 gives relative photon fluxes of 0.1, 1.0, and 0.8 for the transitions to the Γ_1, Γ_4, and Γ_5/Γ_3 final states of $^3T_{1g}$, respectively. These relative values are normalized with respect to the Γ_5 ($^1T_{2g}$) → Γ_4 ($^3T_{1g}$) transition. The transition to the Γ_1 spinor is thus significantly weaker than the transitions to the higher energy spinors of $^3T_{1g}$. The comparison of these values with the analogous bromide spectrum published by Flint et al.[8] is difficult, as the individual luminescence bands are shown on different ordinate scales in ref 8. For Cs_2TeCl_6:Os^{4+},[8] we roughly estimate values of 0.5, 1, and 1.5 for the luminescence bands from Γ_5 ($^1T_{2g}$) to Γ_1 ($^3T_{1g}$), Γ_4 ($^3T_{1g}$), and Γ_5/Γ_3 ($^3T_{1g}$), respectively, again giving the lowest value for the transition to the lowest spinor component of $^3T_{1g}$, in qualitative agreement with the values for the title material.

The relative photon fluxes of radiative transitions starting from the initial level $|i\rangle$ and ending on various final levels $|f\rangle$ are governed by the rate constants k_{fi}:[30]

$$k_{fi} \sim \omega^3 \frac{g_f}{g_i} |\mu_{fi}|^2 \tag{1}$$

where ω corresponds to the transition energy, g_f and g_i are the degeneracies of the final and initial states, respectively, and $\mu_{fi} = \langle f|\mu|i\rangle$ is the transition moment. The energies of the transitions to the ground-state spinor levels Γ_1, Γ_4, and Γ_5/Γ_3 with degeneracies of 1, 3, and 5, respectively, are obtained from Figure 3. Separating out the effects of degeneracies and transition energies in eq 1, we obtain relative $\omega^3 g_f/g_i$ values of 0.8, 1.0, and 0.5 for the transitions from Γ_5 ($^1T_{2g}$) to Γ_1, Γ_4, and Γ_5/Γ_3, respectively, of $^3T_{1g}$. These values are again normalized with respect to the Γ_5 ($^1T_{2g}$) → Γ_4 ($^3T_{1g}$) transition. The comparison with the corresponding experimentally observed photon fluxes of 0.1, 1.0, and 0.8 shows that the values of the Γ_5 ($^1T_{2g}$) → Γ_4 ($^3T_{1g}$) and Γ_5 ($^1T_{2g}$) → Γ_5/Γ_3 ($^3T_{1g}$) transitions are reproduced fairly well by the degeneracy and energy factors of eq 1, but the calculated Γ_5 ($^1T_{2g}$) → Γ_1 ($^3T_{1g}$) value is too big by almost 1 order of magnitude. $|\mu_{fi}|^2$ for the transition to Γ_1 ($^3T_{1g}$) thus appears to be 10 times smaller than the $|\mu_{fi}|^2$ values to Γ_4 ($^3T_{1g}$) and Γ_5/Γ_3 ($^3T_{1g}$). The same qualitative trend is observed in the chloride and bromide analogues. We attempt to rationalize this observation in the following.

Os^{4+} occupies perfectly octahedral sites in Cs_2GeF_6. Therefore all d−d transitions are parity-forbidden and no electric dipole (ED) intensity is expected in the electronic origins of the luminescence transitions in Figure 3. Other, less efficient transition mechanisms are based on magnetic dipole (MD) and electric quadrupole (EQ) interaction. The selection rules collected in Table 5 for the various transition mechanisms within the ligand field states of Os^{4+} transforming as gerade irreducible representations of the O_h point group show that Γ_5 ($^1T_{2g}$) → Γ_1 ($^3T_{1g}$) is MD-forbidden whereas the transitions to Γ_4 ($^3T_{1g}$) and Γ_5/Γ_3 ($^3T_{1g}$) are MD-allowed. The luminescence spectra in Figures 5, 6, and 7 confirm this selection rule. With the exception of the luminescence transition ending on Γ_1 ($^3T_{1g}$), electronic origin intensity is observed for all the luminescence transitions, as described in the detailed analysis of the vibronic structure in section 4.3.

The spectra in Figures 6 and 7 show that the MD origins account for only 10% and 6% of the observed luminescence intensity of the Γ_5 ($^1T_{2g}$) → Γ_4 ($^3T_{1g}$) and Γ_5 ($^1T_{2g}$) → Γ_5/Γ_3 ($^3T_{1g}$) bands, respectively. The biggest part of the observed

---

(28) LIGFIELD ver. 0.92, by J. Bendix; University of Copenhagen.

(29) Bendix, J.; Brorson, M.; Schäffer, C. E. *Inorg. Chem.* **1993**, *32*, 2838.

(30) Brunold, T. C.; Güdel, H. U. In *Inorganic Electronic Structure and Spectroscopy*; Lever, A. B. P., Solomon, E. I., Eds.; John Wiley & Sons: New York, 1999.

Table 4. Spin−Orbital Occupancies of the $(t_{2g})^4$ States of Cs_2GeF_6:Os^{4+} Calculated for $\zeta = 3000$ cm^{-1} and $\zeta = 500$ cm^{-1}, Respectively, as Described in Section 4.2[a]

	j−j coupling			calcd ($\zeta = 3000$ cm^{-1})			calculated (ζ=500 cm^{-1})		
	u'_g (t_{2g})	e''_g(t_{2g})	u'_g (e_g)	u'_g (t_{2g})	e''_g(t_{2g})	u'_g (e_g)	u'_g (t_{2g})	e''_g(t_{2g})	u'_g (e_g)
Γ_1 ($^3T_{1g}$)	4	0	0	3.94	−0.02	0.08	3.48	0.50	0.02
Γ_4 ($^3T_{1g}$)	3	1	0	3.08	0.86	0.06	3.02	0.96	0.02
Γ_5 ($^3T_{1g}$)	3	1	0	2.77	1.19	0.04	2.41	1.57	0.02
Γ_3 ($^3T_{1g}$)	3	1	0	2.74	1.20	0.06	2.41	1.57	0.02
Γ_5 ($^1T_{2g}$)	2	2	0	2.37	1.54	0.09	2.61	1.35	0.04
Γ_3 (^1E_g)	2	2	0	2.46	1.44	0.10	2.63	1.34	0.03
Γ_1 ($^1A_{1g}$)	2	2	0	2.35	1.37	0.28	2.50	1.34	0.16

[a] The Racah and ligand-field parameters were $B = 500$ cm^{-1}, $C = 2380$ cm^{-1}, and $10\,Dq = 24570$ cm^{-1} in both calculations. The j−j coupling values are given for the limit of an infinitively big spin−orbit coupling constant.

Table 5. Selection Rules for Transitions between Electronic States Transforming as Gerade Irreducible Representations of the O_h Point Group[a]

	Γ_1	Γ_2	Γ_3	Γ_4	Γ_5
Γ_1	$v_4\ v_3$	v_6	EQ $v_6\ v_4\ v_3$	MD $v_6\ v_4\ v_3$	EQ $v_6\ v_4\ v_3$
Γ_2	v_6	$v_4\ v_3$	EQ $v_6\ v_4\ v_3$	EQ $v_6\ v_4\ v_3$	MD $v_6\ v_4\ v_3$
Γ_3	EQ $v_6\ v_4\ v_3$	EQ $v_6\ v_4\ v_3$	EQ $v_6\ v_4\ v_3$	MD EQ $v_6\ v_4\ v_3$	MD EQ $v_6\ v_4\ v_3$
Γ_4	MD $v_6\ v_4\ v_3$	EQ $v_6\ v_4\ v_3$	MD EQ $v_6\ v_4\ v_3$	MD EQ $v_6\ v_4\ v_3$	MD EQ $v_6\ v_4\ v_3$
Γ_5	EQ $v_6\ v_4\ v_3$	MD $v_6\ v_4\ v_3$	MD EQ $v_6\ v_4\ v_3$	MD EQ $v_6\ v_4\ v_3$	MD EQ $v_6\ v_4\ v_3$

[a] EQ and MD stand for electric-quadrupole and magnetic-dipole transition mechanisms, respectively, and v_6, v_4, and v_3 indicate the ungerade modes of t_{2u}, t_{1u}, and t_{1u} symmetry, respectively, that can induce electric-dipole intensity to the transitions.

intensity lies in vibronic origins, which acquire ED intensity via Herzberg−Teller coupling[31] and which will be discussed in section 4.3. The MD contribution to the Γ_5 ($^1T_{2g}$) → Γ_4, Γ_5/Γ_3 ($^3T_{1g}$) transitions can thus not explain the order-of-magnitude difference in $|\mu_{fi}|^2$ to the Γ_5 ($^1T_{2g}$) → Γ_1 ($^3T_{1g}$) transition.

The luminescence transitions are both parity- and spin-forbidden, as they involve transitions from singlet to triplet states. Spin−orbit coupling is large for this heavy transition-metal ion, and the ligand-field calculation shows that sizable quintet and singlet character is contained in the ground-state spinor wave functions. It is also this large spin−orbit coupling parameter of 3000 cm^{-1} that leads to the well-separated luminescence transitions to the ground-state spinors depicted in Figure 3. We will therefore focus on the effects of spin−orbit coupling in the following.

The spin−orbit coupling parameters of first-row transition-metal ions range from 100 to 700 cm^{-1},[3] and they are thus smaller than the parameters for interelectronic repulsion and the ligand field. Therefore spin−orbit coupling is treated as a perturbation of the ligand-field states. In third-row transition metals spin−orbit coupling is much bigger and thus comparable in importance to the ligand field and we are in an intermediate coupling regime. For infinitely large spin−orbit coupling we would finally approach the j−j coupling limit.

Due to the comparable importance of spin−orbit and ligand-field interactions, the electronic structure of OsF_6^{2-} shows signatures of both the L−S and the j−j coupling limits. The L−S coupling limit shows up via the spin-selection rule in the absorption intensities of the intraconfigurational transitions in Figure 1. The formally spin-allowed transition to Γ_5/Γ_3 ($^3T_{1g}$) is the dominating band of the absorption spectrum, whereas all the transitions to the singlet states are very weak. Absorption intensities are determined by the wave functions of the states involved in the transitions. Using the singlet, triplet, and quintet contributions to the wave functions of the $(t_{2g})^4$ states given in Table 3, we estimate a difference in intensity of 1 order of magnitude between the formally spin-allowed Γ_1 ($^3T_{1g}$) → Γ_5/Γ_3 ($^3T_{1g}$) and the formally spin-forbidden Γ_1 ($^3T_{1g}$) → Γ_1 ($^1A_{1g}$) transitions.[32] The experimentally observed difference is 2 orders of magnitude, indicating that the multiplicity characters alone cannot fully explain the observed absorption intensities.

The luminescence transitions observed in Figure 3 all end on spinors of the $^3T_{1g}$ ground state, and no insight into the relative $|\mu_{fi}|^2$ of the transitions ending on the individual spinors can be expected from the L−S coupling limit. The j−j coupling limit does give some insight, as will be shown in the following. Under the action of spin−orbit coupling, the t_{2g} orbitals are split into u'_g and e''_g spin−orbitals and the e_g orbitals are transformed into u'_g spin−orbitals. The $^3T_{1g}$ spinors and the intraconfigurationally excited states correspond to the following spin−orbital configurations: Γ_1 ($^3T_{1g}$) ≡ $(u'_g)^4$ $(e''_g)^0$, Γ_4 ($^3T_{1g}$) ≡ $(u'_g)^3$ $(e''_g)^1$, Γ_5 ($^3T_{1g}$) ≡ $(u'_g)^3$ $(e''_g)^1$, Γ_3 ($^3T_{1g}$) ≡ $(u'_g)^3$ $(e''_g)^1$, Γ_5 ($^1T_{2g}$) ≡ $(u'_g)^2$ $(e''_g)^2$, Γ_3 (^1E_g) ≡ $(u'_g)^2$ $(e''_g)^2$, and Γ_1 ($^1A_{1g}$) ≡ $(u'_g)^2$ $(e''_g)^2$, as listed in Table 4. The important result is now the following: In this j−j coupling limit Γ_5 ($^1T_{2g}$) ($(u'_g)^2$ $(e''_g)^2$) → Γ_1 ($^3T_{1g}$) ($(u'_g)^4$ $(e''_g)^0$) is a two-electron transition and thus forbidden. It only gains intensity via the perturbation introduced by interelectronic interactions and the ligand field. Γ_5 ($^1T_{2g}$) ($(u'_g)^2$ $(e''_g)^2$) → Γ_4 ($^3T_{1g}$) ($(u'_g)^3$ $(e''_g)^1$) and Γ_5 ($^1T_{2g}$) ($(u'_g)^2$ $(e''_g)^2$) → Γ_5/Γ_3 ($^3T_{1g}$) ($(u'_g)^3$ $(e''_g)^1$), on the other hand, correspond to one-electron transitions. The observed relative weakness of the Γ_5 ($^1T_{2g}$) → Γ_1 ($^3T_{1g}$) transition can thus be explained with this simple argument.

Table 4 contains calculated spin−orbital occupancies for the states arising from the $(t_{2g})^4$ configuration. The values were obtained as follows: First, the u'_g (t_{2g}), e''_g (t_{2g}), u'_g (e_g) eigenfunctions with respect to the combined action of spin−orbit coupling and the ligand field were determined for a d^1 system, using the OsF_6^{2-} parameter values $\zeta = 3000$ cm^{-1} and $10\,Dq = 24570$ cm^{-1}. Then, the diagonal elements of the spin−orbit coupling and the ligand-field matrices were individually calculated in the basis of the eigenfunctions described above. These values correspond to the contributions that one electron in one of the u'_g (t_{2g}), e''_g(t_{2g}), u'_g (e_g) spin−orbitals makes to the diagonal elements of the spin−orbit coupling and ligand-field matrices of the d^4 system. The diagonal elements of these two

---

(31) Herzberg, G.; Teller, E. *Z. Phys. Chem.* **1933**, *B21*, 410.

(32) The absorption intensity of a transition between $|\Psi_1\rangle = a_1|\text{singlet}\rangle + b_1|\text{triplet}\rangle + c_1|\text{quintet}\rangle$ and $|\Psi_2\rangle = a_2|\text{singlet}\rangle + b_2|\text{triplet}\rangle + c_2|\text{quintet}\rangle$ is assumed to be proportional to $|a_1a_2 + b_1b_2 + c_1c_2|^2 v$, where v corresponds to the energy of the transition. The singlet, triplet, and quintet characters in Table 3 correspond to a_i^2, b_i^2, and c_i^2, respectively.

matrices were calculated for the states of interest in the basis of all the eigenfunctions for the d^4 system, using the OsF_6^{2-} parameter values $\zeta = 3000$ cm^{-1}, $10\,Dq = 24570$ cm^{-1}, $B = 500$ cm^{-1}, and $C = 2380$ cm^{-1}. By decomposing these diagonal elements into the one-electron contributions found for the d^1 system the u'_g (t_{2g}), e''_g (t_{2g}), u'_g (e_g) spin−orbital occupancies were obtained, as collected in Table 4. Table 4 shows that the spin−orbital occupancies are close to the corresponding values of the j−j coupling limit: The u'_g (t_{2g}) occupancies are 3.9, 2.7−3.1, and 2.3−2.5 for the states with u'_g (t_{2g}) populations of 4, 3, and 2, respectively, in the j−j coupling limit. This emphasizes the importance of the selection rules derived in the j−j coupling limit and illustrates an important aspect of the spectroscopy of third-row transition-metal ions such as Os^{4+}. The procedure described above to derive the spin−orbital occupancies neglects higher order terms. This is the reason for the small negative e''_g (t_{2g}) occupancy derived for Γ_1 ($^3T_{1g}$), see Table 4.

Table 4 also gives the spin−orbital occupancies for a reduced spin−orbit coupling constant $\zeta = 500$ cm^{-1}, but otherwhise identical *B*, *C*, and 10 *Dq* values taken from the OsF_6^{2-} calculation. The $\zeta = 500$ cm^{-1} is typical for a first-row transition metal.[3] These latter occupancies are farther away from the j−j coupling limit than the OsF_6^{2-} values, i.e., the ratios of the u'_g (t_{2g}) to e''_g (t_{2g}) occupancies are closer to the 2:1 ratio expected for $\zeta = 0$ cm^{-1}: Whereas the Γ_5 ($^1T_{2g}$) → Γ_1 ($^3T_{1g}$) transition leads to an increase of the u'_g (t_{2g}) occupancy by 1.57 electrons in OsF_6^{2-}, the corresponding increase is only 0.87 electrons for $\zeta = 500$ cm^{-1}. This indicates that the selection rules derived in the j−j coupling limit are of minor importance in the determination of relative photon fluxes in first-row transition metals. Unfortunately, it is difficult to experimentally check this hypothesis, as transitions to different spinor levels strongly overlap in systems with small spin−orbit coupling parameters, see for example the $^1T_{2g} \rightarrow {}^3\,T_{1g}$ luminescence transition of Cs_2NaYCl_6:V^{3+} in ref 33.

The intermediate coupling situation is also consistent with the intensities observed in the absorption spectrum of Cs_2GeF_6:(2% Os^{4+}) depicted in Figure 1. In the formalism of the L−S coupling limit, the absorption bands from the triplet state Γ_1 ($^3T_{1g}$) to the singlet states Γ_5 ($^1T_{2g}$), Γ_3 (^1E_g), and Γ_1 ($^1A_{1g}$) are weak as they are spin-forbidden, whereas the absorption bands to Γ_5/Γ_3 ($^3T_{1g}$) are more intense because they are formally spin-allowed. In the formalism of the j−j coupling limit, the absorption bands from Γ_1 ($^3T_{1g}$) (($u'_g)^4$ $(e''_g)^0$) to Γ_5 ($^1T_{2g}$) (($u'_g)^2$ $(e''_g)^2$), Γ_3 (^1E_g) (($u'_g)^2$ $(e''_g)^2$), and Γ_1 ($^1A_{1g}$) (($u'_g)^2$ $(e''_g)^2$) are weak because they correspond to two-electron transitions, whereas the absorption bands to Γ_5/Γ_3 ($^3T_{1g}$) (($u'_g)^3$ $(e''_g)^1$) are more intense because they correspond to one-electron transitions.

The j−j coupling formalism has already been successfully used to analyze the charge-transfer absorption bands of Cs_2ZrX_6:Os^{4+} (X = Cl, Br).[10] This interpretation was originally postulated[34] because the charge-transfer spectra of Os^{4+} and Ir^{4+} are very similar, despite their different electron configurations $5d^4$ and $5d^5$, respectively. The most intense bands in the Os^{4+} charge-transfer spectra are assigned to symmetry-allowed transitions which correspond to one-electron excitations in the j−j coupling limit. The Coulomb repulsion of the electrons is larger in the $(t_{2g})^4$ excited states of Os^{4+} than in the CT states, in which one electron is formally transferred from a halide MO to the metal d-shell creating a $(t_{2g})^5$ configuration on the metal, giving rise to one single metal state $^2T_{1g}$ which only weakly interacts with the hole created on the ligand. This means that the restrictions imposed by the j−j limit are more severe for the CT transitions of Cs_2ZrX_6:Os^{4+} (X = Cl, Br) than for the transitions within the $(t_{2g})^4$ states.

4.3. Resolved Vibronic Structure. Os^{4+} occupies perfectly octahedral sites in Cs_2GeF_6, and consequently the electronic origins of the intraconfigurational transitions in the absorption and luminescence spectra of Figures 1, 2, and 3 are strictly ED-forbidden. Most of the intensity of the intraconfigurational transitions occurs in exceptionally well-resolved vibronic sidebands. The vibronic sideband intensity mainly arises from the coupling of the electronic transitions to ungerade vibrational modes of the octahedral OsF_6^{2-} unit. These modes dynamically remove the center of inversion around Os^{4+} and thus induce ED intensity for vibronic transitions. Three of the normal modes of the octahedron transform ungerade: the ν_3 (t_{1u}) stretching mode and the ν_6 (t_{2u}) and ν_4 (t_{1u}) bending modes. These modes give rise to vibronic origins, on which progressions in gerade modes can be built. In the Herzberg−Teller formalism[31] the transition moment μ_{ab} induced by coupling of ungerade modes k to the parity-forbidden electronic transition $|a\rangle \rightarrow |b\rangle$ is given as[2]

$$\mu_{ab} = \sum_{k,\Gamma_u} \left(\frac{\langle a|P^k|\Gamma_u\rangle\langle\Gamma_u|\mu|b\rangle}{E_a - E_u} + \frac{\langle a|\mu|\Gamma_u\rangle\langle\Gamma_u|P^k|b\rangle}{E_b - E_u} \right) \tag{2}$$

where the sum runs over the k ungerade normal modes and the ungerade $|\Gamma_u\rangle$ states which are mixed into the gerade states $|a\rangle$ and $|b\rangle$, with the operator

$$P^k = \left(\frac{\partial V}{\partial Q^k}\right)_{Q_0} Q^k \tag{3}$$

describing the derivative of the potential *V* along the Q^k normal coordinates at the equilibrium position Q_0. E_a, E_b, and E_u are the energies of the states $|a\rangle$, $|b\rangle$, and $|\Gamma_u\rangle$, respectively, and μ is the electric dipole moment operator. The observed intensity is proportional to the square of the transition moment. The inverse dependence of the transition moment on the energy difference ΔE between the intensity providing $|\Gamma_u\rangle$ states and the gerade $|a\rangle$ and $|b\rangle$ states is clearly demonstrated in Figure 2. The overall intensity of the intraconfigurational transitions is highest in Cs_2ZrBr_6:Os^{4+}, where the onset of the CT states already occurs at 17000 cm^{-1}. For Cs_2ZrCl_6:Os^{4+}, the intensities are slightly reduced, and for Cs_2GeF_6:Os^{4+} with ΔE values of more than 30000 cm^{-1}, the transitions to Γ_5 ($^1T_{2g}$), Γ_3 (^1E_g), and Γ_1 ($^1A_{1g}$) can barely be observed.

Several attempts have been made in the literature to quantitatively derive the magnitude μ_{ab} for specific modes k.[35−37] The main problem in all these treatments concerns the sum over all $|\Gamma_u\rangle$ states, a sum that cannot be obtained experimentally, because most of the states are not individually observed as the intense, broad transitions in the UV strongly overlap. Severe approximations are usually introduced to bypass these problems. In addition, the derivatives of the potentials along the normal coordinates strongly depend on the force constants used to describe the multidimensional potential surfaces. Despite the detailed experimental information contained in the absorption and luminescence spectra of Figures 1 and 3, we do not have

---

(33) Reber, C.; Güdel H. U. *J. Lumin.* **1988**, *42*, 1.
(34) Jørgensen, C. K. *Mol. Phys.* **1959**, *2*, 309.
(35) Liehr, A. D.; Ballhausen, C. J. *Phys. Rev.* **1957**, *106*, 1161.
(36) Koide, S.; Pryce, M. H. L. *Philos. Mag.* **1958**, *3*, 607.
(37) Acevedo, R.; Flint, C. D. *Mol. Phys.* **1983**, *49*, 1065.
(38) Chodos, S. L.; Black, A. M.; Flint, C. D. *J. Chem. Phys.* **1976**, *65*, 4816.

Table 6. Comparison of Ground-State Vibrational Frequencies of Cs_2OsF_6[20] and Cs_2GeF_6[38a]

	freq (cm^{-1})	
	Cs_2OsF_6	Cs_2GeF_6
ν_1 (a_{1g})	608	610
ν_2 (e_g)	493	472
ν_3 (t_{1u})	547	600
ν_4 (t_{1u})	259/231	350
ν_5 (t_{2g})	217	326
ν_6 (t_{2u})	213	

[a] The normal modes of both compounds are given in O_h notation, even though OsF_6^{2-} is known to occupy a D_{3d} site in Cs_2OsF_6 leading to a splitting of 3-fold degenerate states as observed for ν_4 (t_{1u}).

sufficient data to quantitatively characterize potential surfaces along many coordinates and interactions between highly excited states, which are essential for intensity borrowing. We therefore limit the following to a qualitative analysis.

Table 5 summarizes the electronic and vibronic selection rules for transitions within the ligand-field states of Os^{4+}. The simplest situation among the intraconfigurational transitions $(t_{2g})^4 \rightarrow (t_{2g})^4$ is expected for the transition between the totally symmetric states Γ_1 ($^3T_{1g}$) and Γ_1 ($^1A_{1g}$), which is MD- and EQ-forbidden. Only the t_{1u} modes ν_4 and ν_3 are able to induce ED intensity to the transition, whereas the transition involving ν_6 (t_{2u}) is symmetry-forbidden. The Γ_1 ($^3T_{1g}$) → Γ_1 ($^1A_{1g}$) transition occurs around 22000 cm^{-1} and is shown in the right-hand inset to Figure 1. The two weak and sharp absorption lines at 22040 and 22345 cm^{-1} are immediately assigned to the two vibronic origins involving one quantum of ν_4 (t_{1u}) and ν_3 (t_{1u}), respectively. As expected, no intensity is observed in the region of the electronic origin, which is estimated to occur around 21790 cm^{-1} assuming the vibrational frequencies of ν_4 and ν_3 in Γ_1 ($^1A_{1g}$) of the title compound to be similar to the ground-state frequencies of Cs_2OsF_6.[20] These are 259 cm^{-1}/231 cm^{-1} and 547 cm^{-1}, respectively, as summarized in Table 6. The ν_i modes of Cs_2OsF_6 are given in O_h notation even though Os^{4+} occupies D_{3d} sites.[20] This explains the splitting of the formally 3-fold degenerate mode ν_4 (t_{1u}) into two components, experimentally observed at 259 and 231 cm^{-1}. The fact that no splitting is observed in the two sharp absorption lines proves the exactly octahedral coordination of Os^{4+} in the title material.

The two lowest energy band systems in the absorption spectrum of Figure 1 around 6500 and 13500 cm^{-1} assigned to Γ_5/Γ_3 ($^3T_{1g}$) and Γ_5 ($^1T_{2g}$)/Γ_3 (^1E_g), respectively, show complicated vibronic patterns due to the presence of more than one electronic state. In the following detailed discussion of vibronic structures we will compare these band systems to those in the corresponding luminescence spectra.

The Γ_5 ($^1T_{2g}$) → Γ_1 ($^3T_{1g}$) Transition. This highest energy luminescence band is shown with its corresponding excitation spectrum in Figure 5. The lines in the excitation spectrum appear to be broader than the lines in the luminescence spectrum. Due to the presence of two electronic states around 13500 cm^{-1}, namely, Γ_5 ($^1T_{2g}$) and Γ_3 (^1E_g), a larger number of intense lines are observed in the excitation spectrum than in the luminescence spectrum, which only contains the lines of a single electronic transition, Γ_5 ($^1T_{2g}$) → Γ_1 ($^3T_{1g}$). No intensity is observed in the region of the electronic origin, which is estimated to lie at 12693 cm^{-1} (see arrow in Figure 5), in the middle between the highest energy luminescence and the lowest energy excitation line.

According to the selection rules of Table 5, the electronic transition Γ_5 ($^1T_{2g}$) → Γ_1 ($^3T_{1g}$) is only EQ-allowed. The EQ mechanism does not appear to be efficient enough to generate detectable intensity in the region of the electronic origin. The Γ_5 ($^1T_{2g}$) → Γ_1 ($^3T_{1g}$) transition gains ED intensity by coupling to the three ungerade modes of the octahedron. The three most intense lines at 12486, 12451, and 12144 cm^{-1} in the luminescence spectrum of Figure 5 separated by 207, 242, and 549 cm^{-1}, respectively, from the estimated position of the electronic origin are consequently assigned to the ν_6 (t_{2u}), ν_4 (t_{1u}), and ν_3 (t_{1u}) vibronic origins, respectively. All three enabling modes contribute significantly to the luminescence intensity, and their vibrational frequencies are similar to the ground-state ν_6 (t_{2u}), ν_4 (t_{1u}), and ν_3 (t_{1u}) vibrational frequencies of Cs_2OsF_6,[20] which are 213, 259/231, and 547 cm^{-1}, respectively, see Table 6.

The remaining sharp lines in the luminescence spectrum of Figure 5 correspond to short progressions in gerade modes on the three vibronic origins with energy intervals of 212 and 512 cm^{-1}. These frequencies correspond to the ν_5 (t_{2g}) and ν_2 (e_g) modes of the OsF_6^{2-} octahedron. The corresponding ground-state frequencies in Cs_2OsF_6 are 217 and 493 cm^{-1}, respectively.[20] The Huang−Rhys parameters of these progressions are on the order of 0.1−0.2. All sharp lines in the Γ_5 ($^1T_{2g}$) → Γ_1 ($^3T_{1g}$) luminescence spectrum can thus be unambiguously assigned, see Table 2. The remaining relatively broad and weak bands accompanying the vibronic origins are due to coupling of the electronic transitions to low-frequency lattice modes.

Interestingly, no progression in the totally symmetric ν_1 (a_{1g}) mode with a frequency of 608 cm^{-1} in Cs_2OsF_6 is observed. The progressions in ν_5 (t_{2g}) and ν_2 (e_g) modes indicate Jahn−Teller effects. The small Huang−Rhys factors show that the effects are weak, as expected for states with a low occupancy in the antibonding e_g orbitals, see Table 3.

The lines at 12901, 12950, and 13250 cm^{-1} in the excitation spectrum of Figure 5 are the mirror image to the vibronic origins in the luminescence spectrum. Consequently, they are assigned to the ν_6 (t_{2u}), ν_4 (t_{1u}), and ν_3 (t_{1u}) vibronic origins of Γ_5 ($^1T_{2g}$) with energy differences to the estimated position of the electronic origin of 208, 257, and 557 cm^{-1}, respectively. These vibrational frequencies are similar to those observed for the corresponding luminescence transition, compare Tables 1 and 2. The lines at 13137, 13191, and 13477 cm^{-1} do not have a counterpart in the luminescence spectrum and are consequently assigned to the ν_6 (t_{2u}), ν_4 (t_{1u}), and ν_3 (t_{1u}) vibronic origins of Γ_3 (^1E_g). The vibronic origins are separated by 201, 255, and 541 cm^{-1}, respectively, from the estimated unobserved electronic origin at 12936 cm^{-1}, which is again both MD- and ED-forbidden. Progressions in ν_5 (t_{2g}) and ν_2 (e_g) were observed in the Γ_5 ($^1T_{2g}$) → Γ_1 ($^3T_{1g}$) luminescence spectrum. The corresponding bands in the excitation spectrum are hidden under the relatively broad and intense vibronic origins of Γ_3 (^1E_g). The lines in the energy range between 13500 and 14800 cm^{-1} cannot be assigned unambiguously. They are shown in Figure 5 and in the left inset to the absorption spectrum of Figure 1, and their energetic positions are collected in Table 1. They most probably correspond to the first member of a progression in the totally symmetric ν_1 (a_{1g}) mode built on the vibronic origins of the Γ_3 (^1E_g) state.

The Γ_5 ($^1T_{2g}$) → Γ_4 ($^3T_{1g}$) Transition. The Γ_5 ($^1T_{2g}$) → Γ_4 ($^3T_{1g}$) transition occurs around 9000 cm^{-1} and is displayed in Figure 6. From the previous section we know that the Γ_5 ($^1T_{2g}$) → Γ_1 ($^3T_{1g}$) transition involving a nondegenerate final level shows progressions in the ν_5 (t_{2g}) and ν_2 (e_g) Jahn−Teller modes. By contrast, the Γ_5 ($^1T_{2g}$) → Γ_4 ($^3T_{1g}$) transition involves a 3-fold degenerate final level, which might lead to additional Jahn−Teller effects. It is therefore not surprising to observe a very complicated spectrum with many overlapping lines that cannot be assigned unambiguously, as shown in Figure 6. In the following we assign the most intense features of the spectrum and give tentative explanations for the remaining lines.

Table 5 shows that the $\Gamma_5\ (^1T_{2g}) \rightarrow \Gamma_4\ (^3T_{1g})$ transition is MD-allowed, and the most intense line at 9438 cm^{-1} in Figure 6 is consequently assigned to the electronic origin. This significant intensity for the electronic origin is in contrast to the MD-forbidden $\Gamma_5\ (^1T_{2g}) \rightarrow \Gamma_1\ (^3T_{1g})$ transition discussed above, for which no intensity was observed in the region of the electronic origin. The lines at 9222 and 9185 cm^{-1} are separated by 216 and 253 cm^{-1}, respectively, from the electronic origin and are assigned to the $\nu_6\ (t_{2u})$ and $\nu_4\ (t_{1u})$ vibronic origins, respectively, by comparison with the corresponding vibrational frequencies of Cs_2OsF_6[20] in Table 6. The $\nu_3\ (t_{1u})$ vibronic origin appears to be very weak, and its assignment to the line at 8875 cm^{-1} corresponding to a $\Delta E = 563\ cm^{-1}$ is not unambiguous. This is an important difference to the $\Gamma_5\ (^1T_{2g}) \rightarrow \Gamma_1\ (^3T_{1g})$ transition, where all vibronic origins had comparable intensities, as shown in Figure 5. The groups of lines centered around 8620, 8060, and 7500 cm^{-1} are due to a progression in a 560 cm^{-1} mode on the vibronic origins around 9200 cm^{-1}. The 560 cm^{-1} mode is most likely the totally symmetric $\nu_1\ (a_{1g})$ mode, which has a frequency of 608 cm^{-1} in Cs_2OsF_6.[20] The Huang–Rhys factor of this progression built on the vibronic origins is approximately 0.6 and thus exceptionally high for an intraconfigurational transition. On the other hand, the Huang–Rhys factor of the $\nu_1\ (a_{1g})$ progression built on the electronic origin is very small, $S < 0.1$, with a first member coinciding with the weak 8875 cm^{-1} line, that we tentatively assigned to the $\nu_3\ (t_{1u})$ vibronic origin. This indicates that the larger distortion along the totally symmetric coordinate is induced by Herzberg–Teller coupling of $\Gamma_4\ (^3T_{1g})$ to strongly distorted CT states.

An unambiguous assignment of individual lines to $\nu_5\ (t_{2g})$ and $\nu_2\ (e_g)$ progressions in the $\Gamma_5\ (^1T_{2g}) \rightarrow \Gamma_4\ (^3T_{1g})$ spectrum of Figure 6 is not possible, but we observe luminescence intensity in the expected energy ranges. The first member of the $\nu_5\ (t_{2g})$ progression on the vibronic origins observed around 9200 cm^{-1} is probably responsible for the lines around 9000 cm^{-1}, see the assignment in Figure 6. The lines at 9010 and 8965 cm^{-1} are separated by 212 and 220 cm^{-1}, respectively, from the $\nu_6\ (t_{2u})$ and $\nu_4\ (t_{1u})$ vibronic origins. These frequencies are similar to the $\nu_5\ (t_{2g})$ frequency of 217 cm^{-1} observed in Cs_2OsF_6.[20] The $\nu_2\ (e_g)$ progression could explain the luminescence intensity observed around 8700 cm^{-1}, which is separated by roughly 500 cm^{-1} from the $\nu_6\ (t_{2u})$ and $\nu_4\ (t_{1u})$ vibronic origins. The $\nu_5\ (t_{2g})$ and $\nu_2\ (e_g)$ progressions on the electronic origin might explain part of the intensity observed around 9200 and 8950 cm^{-1}, respectively.

In contrast to the electronic origin, many of the vibronic lines are resolved into several components at our best experimental resolution. This splitting was not observed for the $\Gamma_5\ (^1T_{2g}) \rightarrow \Gamma_1\ (^3T_{1g})$ transition and is therefore attributed to the combination of multidimensional distortions of the emitting state $\Gamma_5\ (^1T_{2g})$ relative to the final degenerate state $\Gamma_4\ (^3T_{1g})$.

The $\Gamma_5\ (^1T_{2g}) \rightarrow \Gamma_5/\Gamma_3\ (^3T_{1g})$ Transition. The $\Gamma_5\ (^1T_{2g}) \rightarrow \Gamma_5/\Gamma_3\ (^3T_{1g})$ luminescence transition occurs around 6500 cm^{-1} and is shown in Figure 7 together with the corresponding absorption spectrum. Electronic transitions to both the $\Gamma_5\ (^3T_{1g})$ and $\Gamma_3\ (^3T_{1g})$ spinor levels are MD-allowed, and we observe the electronic origins at 6740 and 6693 cm^{-1}, respectively. The energy difference between the two states is thus only 47 cm^{-1}, which complicates the task of assigning the observed lines. In addition, both the $\Gamma_5\ (^1T_{2g})$ emitting state and the degenerate $\Gamma_5\ (^3T_{1g})$ and $\Gamma_3\ (^3T_{1g})$ final states are susceptible for Jahn–Teller effects. Therefore the assignment is not entirely unambiguous, as will be pointed out in the following.

The lines in the luminescence spectrum of Figure 7 at 6552, 6487, and 6186 cm^{-1} are separated by 208, 253, and 554 cm^{-1} from the $\Gamma_5\ (^3T_{1g})$ electronic origin. They are unambiguously assigned to the $\nu_6\ (t_{2u})$, $\nu_4\ (t_{1u})$, and $\nu_3\ (t_{1u})$ vibronic origins of $\Gamma_5\ (^3T_{1g})$. The vibrational frequencies are similar to the $\nu_6\ (t_{2u})$, $\nu_4\ (t_{1u})$, and $\nu_3\ (t_{1u})$ frequencies of Cs_2OsF_6, which are 213, 259/231, and 547 cm^{-1}, respectively.[20] The $\nu_6\ (t_{2u})$ and $\nu_4\ (t_{1u})$ vibronic origins are considerably more intense than the $v_3\ (t_{1u})$ vibronic origin.

The lines at 6513 and 6471 cm^{-1} are separated by 180 and 222 cm^{-1}, respectively, from the $\Gamma_3\ (^3T_{1g})$ electronic origin. Although these observed intervals are significantly smaller than for the luminescence transition to $\Gamma_5\ (^3T_{1g})$, they are tentatively assigned to the $\nu_6\ (t_{2u})$ and $\nu_4\ (t_{1u})$ vibronic origins of $\Gamma_3\ (^3T_{1g})$. No intense $\nu_3\ (t_{1u})$ vibronic origin is observed for $\Gamma_3\ (^3T_{1g})$. Many of the lines around 6500 cm^{-1} are split into several components under increased spectral resolution. The lines around 6300 and 6100 cm^{-1} are assigned as the first and second members of a $\nu_5\ (t_{2g})$ progression on the $\nu_6\ (t_{2u})$ and $\nu_4\ (t_{1u})$ vibronic origins around 6500 cm^{-1}, see the assignment in Figure 7. No appreciable intensity is observed around 6000 cm^{-1}, where the first member of the $\nu_2\ (e_g)$ progression on the $\nu_6\ (t_{2u})$ and $\nu_4\ (t_{1u})$ vibronic origins is expected. We thus conclude that the distortion of the $\Gamma_5/\Gamma_3\ (^3T_{1g})$ final states along the ν_2 coordinate is weak and similar to the one in the $\Gamma_5\ (^1T_{2g})$ emitting state. The lines around 5900 cm^{-1} finally correspond to the first members of a progression in the totally symmetric $\nu_1\ (a_{1g})$ mode on the 6500 cm^{-1} vibronic origins.

The absorption $\Gamma_1\ (^3T_{1g}) \rightarrow \Gamma_5/\Gamma_3\ (^3T_{1g})$ ends on the same final level as this low-energy luminescence band. In the bottom part of Figure 7 the absorption is shown on a reversed energy axis. The energy range shown has the same width as the luminescence spectrum in the top part, and the energy window is chosen to show the electronic origins in absorption and luminescence at identical horizontal positions in the figure. No absorption is detected at the positions of the electronic origins because both transitions $\Gamma_1\ (^3T_{1g}) \rightarrow \Gamma_5\ (^3T_{1g})$ and $\Gamma_1\ (^3T_{1g}) \rightarrow \Gamma_3\ (^3T_{1g})$ are MD-forbidden. The vibronic sidebands of the absorption and luminescence spectra occur at similar energy differences from the electronic origins. Their exact positions are not identical, though. This indicates that slightly different parts of the $\Gamma_5/\Gamma_3\ (^3T_{1g})$ potential surfaces are probed by the two experiments. The luminescence starts from the potentially Jahn–Teller distorted degenerate $\Gamma_5\ (^1T_{2g})$ emitting state, whereas the absorption starts from the nondegenerate $\Gamma_1\ (^3T_{1g})$ ground state.

The $\Gamma_5\ (^1T_{2g}) \rightarrow \Gamma_1/\Gamma_4/\Gamma_5/\Gamma_3\ (^3T_{1g})$ luminescence spectra of Os^{4+} doped into the isostructural Cs_2TeCl_6 and Cs_2SnBr_6 hosts have been reported.[8] In these spectra, the resolution is much poorer and many of the details presented above for Cs_2GeF_6:Os^{4+} are not visible. This is partially due to the lower vibrational frequencies of chloride and bromide lattices, leading to less separated vibronic lines. The relative intensities of the vibronic origins compared to the electronic origin intensities are considerably higher in the chloride and bromide spectra than in the spectra of the title material, which again is explained by the lower energy of the intensity providing CT states in the former, leading to smaller ΔE values in eq 2 describing the magnitude of the transition moments induced by Herzberg–Teller coupling.[31]

5. Conclusions

We have synthesized the title compound and measured single-crystal absorption, excitation, and luminescence spectra. The combination of all spectroscopic data allows us to determine the detailed ligand-field parameters necessary to characterize the electronic structure. The effects of the ligand field, spin–orbit coupling, and Coulomb repulsion are comparably large, resulting in an intermediate coupling situation. As an important consequence, the overall electronic structure of the title material cannot be described in a single coupling limit but has to be simultaneously analyzed from the perspectives of the cubic strong field and the L–S and j–j coupling limits. Selected observables revealing the importance of the various coupling limits in the description of the electronic structure of Cs_2GeF_6:Os^{4+} are the following. The near-IR and visible spectral range of the absorption spectrum is dominated by intraconfigurational $(t_{2g})^4 \rightarrow (t_{2g})^4$ transitions, a consequence of the strong ligand field. The large spin–orbit coupling is evidenced by the splitting of the $^3T_{1g}$ ground state of 6000 cm^{-1}. Consequently, the wave functions of the ligand-field states are expected to be characterized by a strong mixing between L–S states of different multiplicities. Despite this strong mixing, *S* still appears to be a good quantum number to describe the observed relative absorption intensities of transitions within the $(t_{2g})^4$ configuration. The formally spin-allowed absorptions to Γ_5/Γ_3 ($^3T_{1g}$) dominate the absorption spectrum, whereas the formally spin-forbidden transitions to the singlet states are all very weak, in agreement with the spin-selection rule derived in the L–S coupling limit. On the other hand, relative intensities of the luminescence transitions ending on the various ground-state spinors can be rationalized with the selection rules derived in the j–j coupling limit. This list nicely illustrates the intermediate coupling in third-row transition-metal ions. Depending on the observable, we recognize features corresponding to different coupling limits. We believe that this behavior, which may appear contradictory at some points, is typical for systems with intermediate coupling, such as third-row transition-metal ion complexes. This is in contrast to first-row transition-metal ions, in which Coulomb repulsion and the ligand field clearly dominate, and consequently, spin–orbit coupling is treated as a weak perturbation of the ligand-field states.

The Γ_5 ($^1T_{2g}$) $\rightarrow$ $\Gamma_1/\Gamma_4/\Gamma_5/\Gamma_3$ ($^3T_{1g}$) luminescence spectrum discussed in section 4.3 reveals extensive, well-resolved vibronic structure. The main intensity of all the transitions lies in vibronic origins involving the ungerade local modes of the OsF_6^{2-} octahedron. Progressions in gerade modes on the vibronic and electronic origins are only short. A complete vibronic assignment of the Γ_5 ($^1T_{2g}$) $\rightarrow$ Γ_1 ($^3T_{1g}$) transition is possible, revealing the coupling to ν_2 (e_g) and ν_5 (t_{2g}) Jahn–Teller modes. Also in the Γ_5 ($^1T_{2g}$) $\rightarrow$ Γ_4 ($^3T_{1g}$) and Γ_5 ($^1T_{2g}$) $\rightarrow$ Γ_5/Γ_3 ($^3T_{1g}$) transitions, the main features are understood. Due to the complexity arising from multidimensional distortions of the degenerate initial and final states, a complete vibronic assignment of the individual lines in the latter two luminescence multiplets is not possible.

Acknowledgment. This work was financially supported by the Swiss National Science Foundation. We thank B. Lorenzen and W. Preetz for providing us the K_2OsF_6. We are greatly indebted to Jesper Bendix for providing his LIGFIELD program[28] and for many fruitful discussions. C.R. thanks the Hans Sigrist foundation for sabbatical support.

IC001369S